Scripta Materialia 187 (2020) 268–273

Contents lists available at ScienceDirect

Scripta Materialia

journal homepage: www.elsevier.com/locate/scriptamat

Spontaneous magnetic bubbles and large topological Hall effect in $Mn_{3-x}Fe_xSn$ compound

Jun Liu[a,b], Shulan Zuo[c], Hang Li[a,b], Yanli Liu[a,b], Xinqi Zheng[d], Ying Zhang[a], Tongyun Zhao[a], Fengxia Hu[a,b], Jirong Sun[a,b], Baogen Shen[a,b,*]

[a] State Key Laboratory of Magnetism, Institute of Physics, Chinese Academy of Sciences, Beijing 100190, China
[b] University of Chinese Academy of Sciences, Beijing 100049, China
[c] School of Materials Science and Engineering, Beihang University, Beijing 100191, China
[d] School of Materials Science and Engineering, University of Science and Technology Beijing, Beijing 100083, China

ARTICLE INFO

Article history:
Received 31 March 2020
Revised 12 June 2020
Accepted 13 June 2020
Available online 23 June 2020

Keywords:
Magnetic domains
Transport properties
Lorentz transmission electron microscopy

ABSTRACT

Magnetic and transport properties as well as magnetic domain structures have been investigated in a hexagonal polycrystalline $Mn_{2.1}Fe_{0.9}Sn$ compound. The in-situ observation of Lorentz transmission electron microscopy shows that spontaneous magnetic bubbles owing a pair of Bloch lines and biskyrmions consisting of two skyrmions of opposite spin helicities coexist in this compound at low temperature. A large topological Hall resistivity up to about 9 μΩ·cm at 50 K has been found owing to the formation of noncoplanar spin textures deriving from the competition among magnetocrystalline anisotropy, antiferromagnetic coupling, and ferromagnetic interaction.

Topological spin textures, such as magnetic skyrmions, bubbles, and vortex, have drawn widespread attention from researchers due to the potential application in spintronics devices [1-8]. Generally, skyrmions with nanoscale have a smaller size than conventional bubbles, which makes skyrmion materials become an ideal candidate in future high-density magnetic memory devices [1-3]. Most of such unique magnetic nanodomains have been recently discovered in noncentrosymmetric crystal structure such as chiral magnets MnSi [1], FeCoSi [2], FeGe [3] and so on. In these systems, Dzyaloshinsky-Moriya interaction (DMI) deriving from lack of centrosymmetry is regarded as an important role to stabilize the spin configuration of skyrmions. Afterwards, it has also been observed in centrosymmetric magnets with uniaxial magnetic anisotropy, such as $BaFe_{1-x-0.05}Sc_xMg_{0.05}O_{19}$ [4], $La_{2-2x}Sr_{1+2x}Mn_2O_7$ [5], MnNiGa [6,9] and Fe_3Sn_2 [7]. In these materials, the formation of skyrmions is attributed to the competition between magnetic dipole interplay and uniaxial magnetic anisotropy.

The compound Mn_3Sn is a DO_{19}-type hexagonal antiferromagnetic material with an inverse triangle spin configuration [10,11]. In 2015, Nakatsuji et al. reported a large anomalous Hall effect (AHE) in this compound at room temperature employing Berry-phase concepts, which received widely concern from researchers [10]. Subsequently, many interesting other physical features such as Weyl fermions [12,13], anomalous Nernst effect [14,15], large magneto-optical Kerr effect [16], and THz emission [17], were reported in the Mn_3Sn alloy. However, according to previous literature, the easy magnetic axis of the Mn_3Sn alloy lies in the hexagonal plane rather than uniaxial magnetic anisotropy [10,11]. It is contradictory for the Mn_3Sn alloy as potential magnetic skyrmions or bubbles-based materials with uniaxial magnetic anisotropy, which can introduce noncolinear spin textures by the competition between magnetic dipole interaction and magnetic anisotropy [6]. Meanwhile, the Fe_3Sn alloy as a ferromagnetic material has a same hexagonal structure with the Mn_3Sn alloy [18,19]. As a result, it is natural to think that a portion of Mn atoms in Mn_3Sn alloy are substituted by Fe atoms, which will cause the introduction of ferromagnetic exchange interaction in the alloy. In this way, on one hand, the large moment of Fe atom will improve the magnetization of the $(Mn,Fe)_3Sn$ alloy, which makes the sample transform from antiferromagnetism to ferromagnetism or ferrimagnetism. On the other hand, it is possible that the moments of Mn atoms begin to incline, resulting in the formation of noncollinear or noncoplanar magnetic structures. Hori [20] and Felez [21] reported the control of magnetic properties and Curie temperature by Fe content in Mn_3Sn alloy. But there are few reports on the corresponding transport properties and magnetic domain structure for $(Mn,Fe)_3Sn$ alloys. In this paper, $Mn_{3-x}Fe_xSn$ alloys with $x = 0.9$ was selected to study these in detail. The crystalline structure, magnetic transition, magnetic domain structure and magneto-transport properties

* Corresponding author.
E-mail address: shenbaogen@yeah.net (B. Shen).

https://doi.org/10.1016/j.scriptamat.2020.06.034
1359-6462/

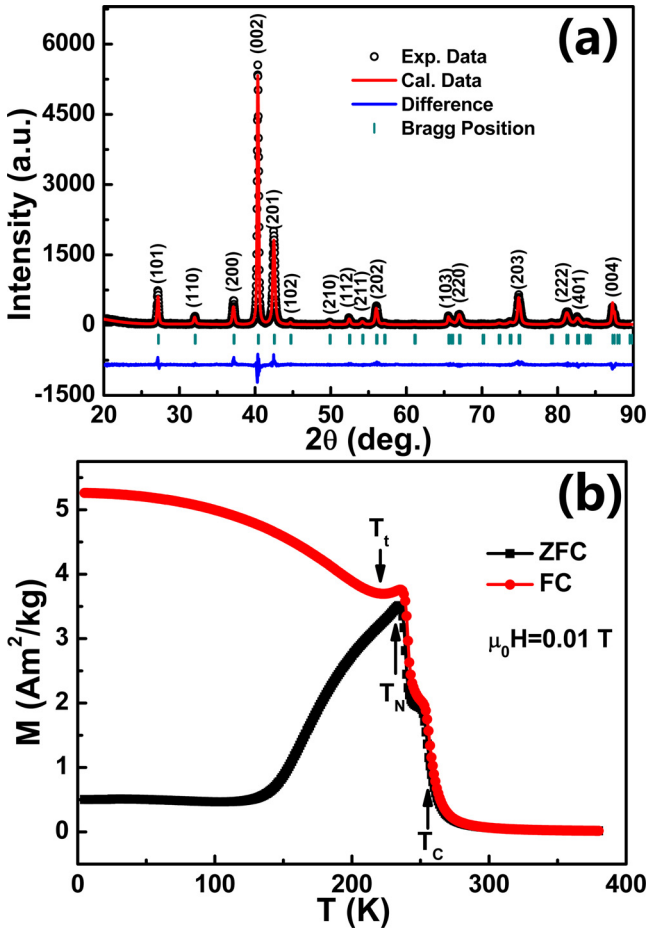

Fig. 1. (a) XRD patterns and Rietveld refined results of $Mn_{2.1}Fe_{0.9}Sn$ compound measured at room temperature. The experiment data are indicated by hollow circles; the calculated profile is the continuous red line overlying them; the short vertical green lines indicate the angular positions of the Bragg peaks; the lower blue curve shows the difference between the observed and calculated intensity. (b) Temperature dependence of ZFC and FC magnetization under a magnetic field of 0.01 T of $Mn_{2.1}Fe_{0.9}Sn$ compound. (For interpretation of the references to colour in this figure legend, the reader is referred to the web version of this article.)

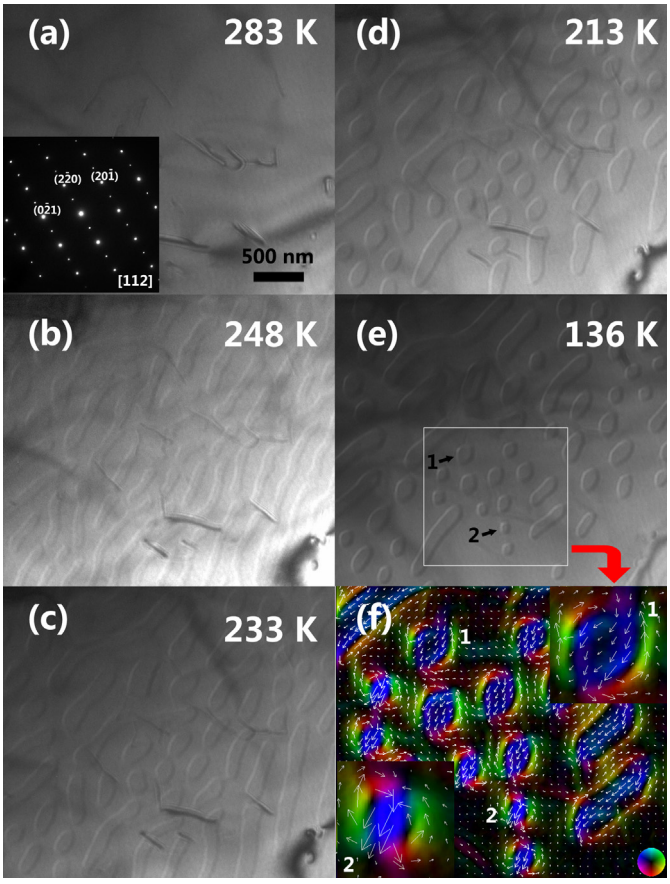

Fig. 2. (a)-(e) The evolution of magnetic domain structures for $Mn_{2.1}Fe_{0.9}Sn$ thin plate observed by means of LTEM as the temperature was decreased from 283 K to 136 K at zero magnetic field. The inset of Fig. 2(a) shows the selected-area electron diffraction (SAED) pattern. (f) Corresponding domain structures of the selected area in Fig. 2(e) (white rectangle) obtained by the QPt software based on the transport of intensity equation (TIE). White arrows represent the direction of in-plane magnetic induction, and the dark color stands for the magnetic induction along the out-of-plane direction. "1″ and "2″ display the type-II magnetic bubble and biskyrmion.

of the alloy were investigated. It was found that the alloy exists spontaneous magnetic bubbles and biskyrmions, which was further confirmed by large topological Hall effect at low temperature.

A polycrystalline $Mn_{2.1}Fe_{0.9}Sn$ ingot was prepared by arc-melting method under protection of high-purity argon atmosphere. Homogeneity for the sample was ensured by turning and re-melting for several times. The sample was annealed at 1073 K for two weeks and quenched in liquid nitrogen. The phase component and the crystalline structure were characterized by the X-ray diffraction (XRD) measurement using a Rigaku D/Max-2400 diffractometer with Cu Kα radiation (λ=1.54056 Å). The thin plate for Lorentz transmission electron microscopy (LTEM) observation was prepared by traditional mechanical polishing and argon ion milling. A JEOL-dedicated LTEM was used to image magnetic domain configuration with almost no remnant magnetic field near the sample. A liquid-nitrogen TEM sample holder (from room temperature to about 100 K) was employed to make the in-situ cooling experiment. Magnetic properties were examined using a superconducting quantum interference device magnetometer (SQUID-VSM). The polycrystalline sample was milled into a 2.5 × 1 × 0.06 mm^3 to measure transport properties by a Quantum Design Physical Property Measurement System (PPMS).

Fig. 1(a) exhibits the typical powder XRD pattern of the $Mn_{2.1}Fe_{0.9}Sn$ alloy and Rietveld refined result at room temperature. All of diffraction peaks of the sample can be identified as Mn_3Sn-type structure (space group: P63/mmc, JCPDS PDF # 21–0558), and every diffraction peak is marked with corresponding crystal plane index. The lattice parameters from the result of Rietveld refined are a = 0.5588 nm and c = 0.4468 nm, slightly smaller than Mn_3Sn resulting from the Fe substitution [11]. It should be noted that the main peak in XRD pattern is the (002) peak rather than the (201) peak, which means a strong texture along the [002] crystal orientation in the sample.

The temperature dependence of magnetization of the $Mn_{2.1}Fe_{0.9}Sn$ alloy from 5 K to 380 K measured at a magnetic field of 0.01 T is displayed in Fig. 1(b). According to the ZFC-FC curves, it can be seen that the alloy undergoes three obvious magnetic transitions in the range of measured temperature. As the temperature decreases, the alloy experiences firstly a transition from paramagnetism to ferromagnetism at 257 K (T_C). When temperature drops down to 235 K (T_N), two cusps appear in both ZFC and FC curves, which presents an antiferromagnetic transition. After that, the magnetization continues to increase in FC curve below 220 K (T_t), which can be regarded as the rotation of magnetic moments (spin reorientation) due to the enhancement of magnetocrystalline anisotropy with decreasing temperature. As a whole, the ground state of sample is the coexistence of FM and AFM phases at low temperature, which is consistent with previous conclusion [20].

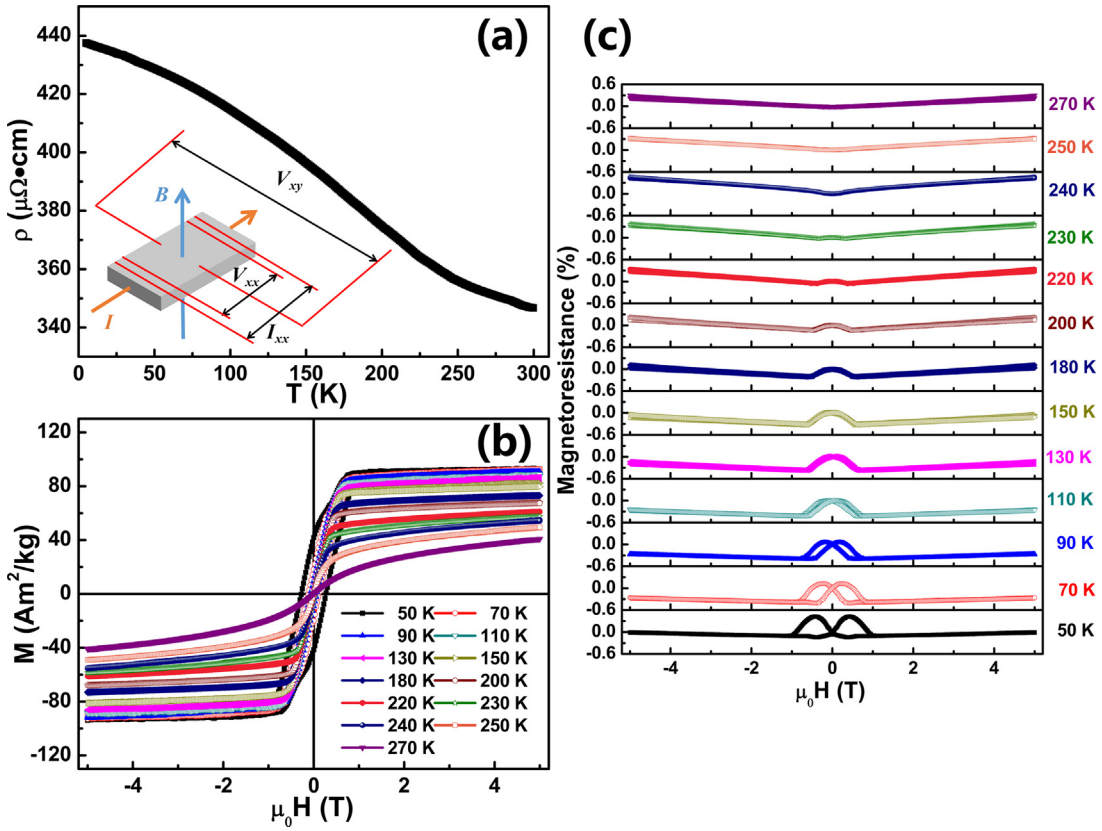

Fig. 3. (a) The temperature dependence of longitudinal resistivity of $Mn_{2.1}Fe_{0.9}Sn$ compound under zero field. The inset shows the schematic diagram of measurement. (b) Hysteresis loops sweeping field between 5 T and −5 T at different temperatures from 50 K to 270 K. (c) Magnetic field dependence of magnetoresistance measured under the same condition. (For interpretation of the references to colour in this figure legend, the reader is referred to the web version of this article.)

To explore the temperature dependence of magnetic domain evolution in the $Mn_{2.1}Fe_{0.9}Sn$ alloy, the in-situ observation was carried out in the temperature range of 136–293 K at zero field by using LTEM. It should be mentioned that the sample of LTEM observation was cut from the direction perpendicular to the texture of the ingot. Fig. 2(a)-(f) displays the under-focused LTEM images at different temperature. Magnetic domain walls are imaged as bright or dark contrast in the Fresnel mode. The selected-area electron diffraction (SAED) patterns at 293 K suggest that the observed grain is along the [112] zone axis (shown in the inset of Fig. 2(a)). The result of XRD (Fig. 1(a)) shows that the sample has a preferred growth along with [002] crystal orientation. Therefore, the surface of single grain we observed is adjacent to ab-plane.

As it can be seen from Fig. 2, there is no magnetic contrast by reason of paramagnetic state at 283 K (above T_C, Fig. 2(a)). When the temperature decreases to 248 K (below T_C, Fig. 2(b)), weak magnetic contrast appeared and developed a large number of spontaneous stripe domains with an average periodicity of about 50 nm. The stripe domains become wide and break gradually into fragments in thicker area of the thin plate, while there are some magnetic bubbles in thinner region of it with decreasing temperature to 233 K (below T_N, Fig. 2(c)). As the temperature decrease to 213 K (below T_t, Fig. 2(d) further, the large bubbles become smaller. We employed commercial Qpt software on the basis of the transport of intensity equation (TIE) to obtain the high-solution in-plane magnetization distribution map of domain structures at 136 K (Fig. 2(e)), which is shown in Fig. 2(f). The white arrows stand for in-plane magnetization distribution while the black area presents out-of-plane magnetization of the sample. The result of TIE analysis reveals that domain structures mainly exist two spin textures. One is the conventional type-II bubble (mark as “1”) deriving from the pinched-off stripes. The bubble external consists of a pair of semicircular rings with opposite winding spins and its core shows the out-of-plane magnetization (black area), separated by a pair of Bloch lines. Consequently, the topological number N_S is zero [5]. Another is the biskyrmion (mark as “2″) composed of two skyrmions with opposite helicities, namely clockwise and anticlockwise spin curls. According to the direction of the magnetization at the core of two skyrmions, we can ensure that two skyrmions, have the same core spin directions parallel to the external magnetic field, hence, the topological number N_S is two, similar with the previous reported [5,6,9,22]. Throughout the cooling process, the magnetic domain structure has undergone a change from stripe domain to conventional type-II magnetic bubbles, then to biskyrmion state, and to vanish finally. The reason for discrepant magnetic domain structures in the process of cooling is likely to the competition between magnetic dipole interaction and the change of magnetocrystalline anisotropy [7].

For the interesting phenomenon exhibited in magnetic domain structures, we investigate the magnetic transition behavior by measurement of magnetization and transport properties of $Mn_{2.1}Fe_{0.9}Sn$ alloy. Fig. 3(a) shows the temperature dependence of resistivity ρ under zero magnetic field from 5 K to 300 K. It can be seen that ρ decreases slightly from 437 μΩ·cm at 5 K to 347 μΩ·cm at 300 K, indicating the sample presents the nonmetallic behavior. The observed conducting character is different from the metallic feature of Mn_3Sn [10], Fe_3Sn [23], Fe_3Sn_2 [24] as well as Mn_2PtSn [25,26], but analogous to the phenomenon in Mn_2(Pt,Co)Sn compound [27]. Considering that the sample is polycrystalline, the scatting effect between grain boundaries plays a significant role in resistivity [28,29]. For this trend of resistivity change, the empirical rule of Mooij thinks that metallic materials with electrical

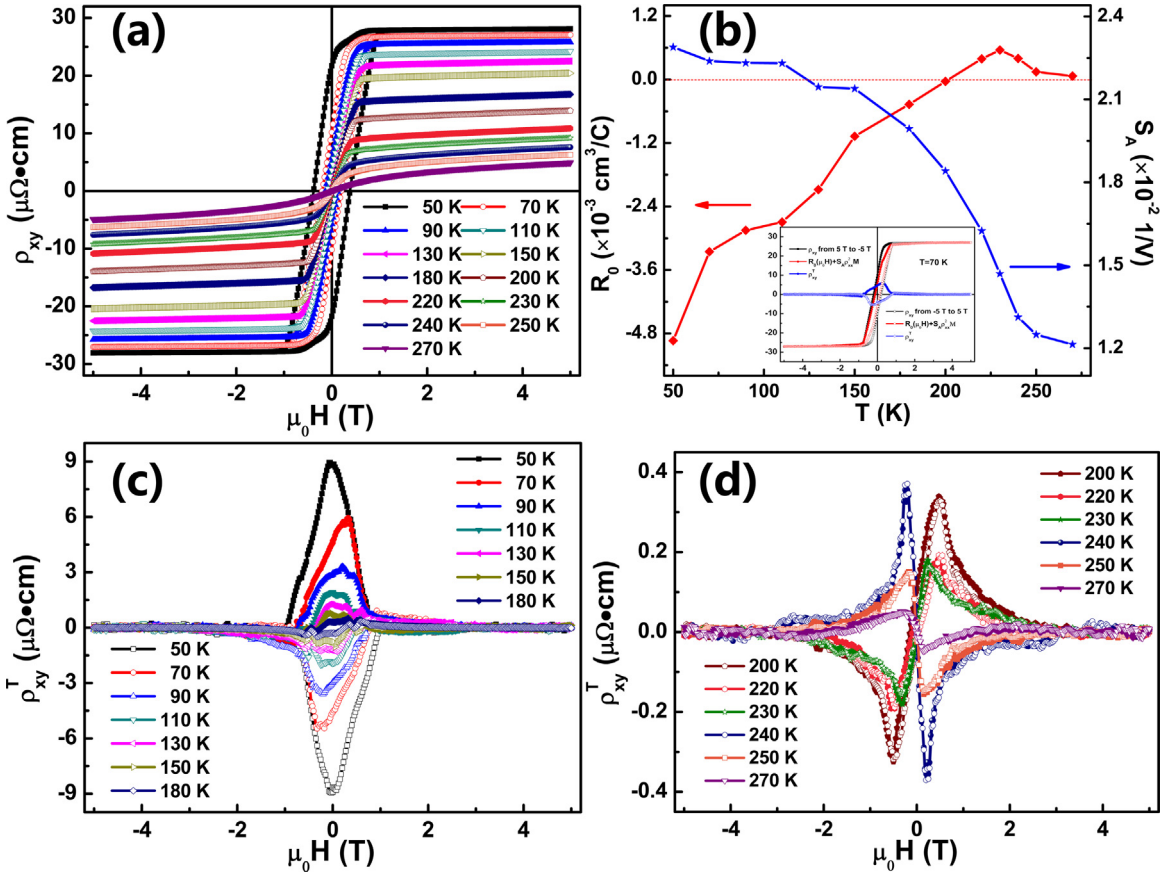

Fig. 4. (a) Hall resistivies ρ_{xy} as a function at various temperatures ranging from 50 K to 270 K for $Mn_{2.1}Fe_{0.9}Sn$ compound. (b) Temperature dependence of ordinary Hall coefficient R_0 (red diamonds) and scaling factor S_A (blue stars) related to ordinary Hall coefficient. The inset shows the getting process of ρ^T_{xy} at 70 K. The black squares show the measured ρ_{xy}-H curve. The red circles are the calculated $R_0(\mu_0 H) + S_A\rho^2_{xx}M$. The blue diamonds are difference standing for the value of ρ^T_{xy}. The closed and open symbols represent ρ_{xy} sweeping from +5 T to −5 T and from −5 T to +5 T, respectively. The obtaining ρ^T_{xy} from (c) 50 K to 180 K, and from (d) 200 K to 270 K. (For interpretation of the references to colour in this figure legend, the reader is referred to the web version of this article.)

resistivity value above 150 μΩ·cm usually show a negative temperature coefficient (NTC) for all temperatures due to chemical disorder [30]. Moreover, nanoscale and noncollinear spin disturbances have a contribution to this non- behavior [26]. Another possible reason is that the electronic band structure is likely to be changed due to the substitution of Fe content compared with Mn_3Sn, which makes the $Mn_{2.1}Fe_{0.9}Sn$ alloy present the feature of half-metal [29].

Fig. 3(b) and Fig. 3(c) display the magnetic field dependence of magnetic hysteresis loops and longitudinal resistivitiy ρ_{xx} at different temperatures measured with applied fields up to 5 T. As shown in Fig. 3(b), the magnetization at 7 T decreases with the increase of temperature from 50 K to 300 K, manifesting that the sample has been transformed into an ordinary ferromagnetic material. It should be stressed that the magnetization cannot be totally saturated under high field, which is stemming from the existence of AFM phase in the sample [31]. The alloy has an obvious coercivity below 220 K, indicating the strong magnetocrystalline anisotropy at low temperature [32], which is consistent with the analysis of M-T curves above. It is noteworthy that the magnetization curve at 50 K appears the “collapse” indicating the weak exchange-coupling between grains similar with the phenomenon in Nd-Fe-B permanent materials [33]. In addition, we can use the formula MR=[ρ_{xx}(H)-ρ_{xx}(0)]/ρ_{xx}(0) × 100% to calculate the value of magnetoresistance (MR), as depicted in the Fig 3(c). A butterfly-shaped MR curve, where two peaks value correspond to two coercivity fields [34], can be observed below 220 K. It is worth noting that the coercivity field in MR-H curves is greater than in magnetization curves at same temperature, and the difference of coercivity field gradually decreases to zero with increasing temperature to 220 K. This phenomenon is probably resulting from the inconsistence of magnetic moments reversal due to the coexistence of FM and AFM phases at low temperature, when applying the reversal field. In addition, the sign of MR is positive at 50 K under lower field and gradually transforms into negative values in the high field, exhibiting the complex magnetic structure. The sign changes from positive to negative ranging from 70 K to 230 K under lower field. When the temperature is higher than 240 K, it becomes positive again. The change of sign of MR in this process may result from the rotation of magnetic moments and AFM phase transition with temperature [35].

Magnetic field dependence of Hall resistivity ρ_{xy} under the same measurement condition are displayed in Fig. 4(a). The ρ_{xy}-H curves also show the hysteresis effect below 220 K and the value of ρ_{xy} decreases with increasing the temperature, which is coincide with the result of ρ-T curve above. In general, normal Hall resistivity ρ^N_{xy} has a linear relationship with applied magnetic field H, and anomalous Hall resistivity ρ^A_{xy} is proportional to the magnetization. Hence, the total ρ_{xy} can be expressed as $\rho_{xy} = \rho^N_{xy} + \rho^A_{xy} = R_0(\mu_0 H) + S_A\rho^2_{xx}M$, where R_0 is the normal Hall coefficient, S_A stands for the scaling coefficient independent of the field H [32]. Considering that there is likely to exist topological Hall resistivity ρ^T_{xy} in the sample, and it will disappear under high magnetic field

due to the consistent arrangement of magnetic moments [25,35]. Therefore, we employ the formula $\rho_{xy}/(\mu_0 H = R_0 + S_A \rho_{xx}^2 M/(\mu_0 H)$ to depict the $\frac{\rho_{xy}}{(\mu_0 H)} - \rho_{xx}^2 M/(\mu_0 H)$ curves which should present the linear relationship. The value of R_0 and S_A can be obtained from the intercept and slop of linear curves, respectively, as shown in Fig. 4(b). The value of R_0 is negative at 50 K, and then changes to positive at 220 K, manifesting the type of conduction transforms from electron to hole. Liu et al. reported that the ribbon of Mn_2PtSn also shows the change of charge carrier type. They attributed this phenomenon to the competition between two conducting charge carriers [25]. Besides, we also think that the change of magnetic structure results in the alteration of band structure adjacent to 220 K. Hence, corresponding magnetic structure needs to be studied further. In addition, scaling coefficient S_A is estimated to about 0.02 V^{-1}, lying in range of the order of 0.01–0.1 V^{-1} for FMs [10].

Topological Hall resistivity ρ_{xy}^T extracted from total ρ_{xy} is separately plotted in Fig. 4(c) (50 K-180 K) and Fig. 4(d) (200 K-270 K) so as to compare ρ_{xy}^T having the same order of magnitude. As it is seen from Fig. 4(c) and 4(d), a large ρ_{xy}^T about near 9 μΩ·cm is found in the sample at 50 K, which is three times larger than the maximum value of Mn_3Sn [32]. And then it damps promptly to 0.17 μΩ·cm at 230 K. When the temperature rises to 240 K, the sign of ρ_{xy}^T changes from positive to negative. At the same time, ρ_{xy}^T inversely increases to 0.36 μΩ·cm and then gradually decreases to 0.04 μΩ·cm at 270 K. We speculate that topological Hall effect owes to the formation of noncoplanar spin textures, which is deriving from the competition among magnetocrystalline anisotropy, antiferromagnetic coupling and ferromagnetic interaction. When the temperature is lowed, magnetic moments with originally colinear or coplanar alignment produce a large rotation in virtue of strong magnetocrystalline anisotropy. It causes the formation of noncoplanar spin textures, further inducing the Berry phase to the conduction electrons, which contributes to the Hall resistivity [35]. As a result, ρ_{xy}^T has a large value up to 9 μΩ·cm at 50 K. Magnetocrystalline anisotropy gradually declines with increasing the temperature to 220 K, which weakens the competition with two other interactions, thus reducing the value of ρ_{xy}^T to 0.19 μΩ·cm. When the temperature rises to 230 K further, the coupling among three interactions falls to the lowest level, showing the minimum ρ_{xy}^T to 0.17 μΩ·cm. As the temperature is higher than 240 K, AFM phase in the sample transforms to PM state, only two interactions contribute to the formation noncoplanar spin textures, which could lead to the alteration of sign of ρ_{xy}^T. Meanwhile, when temperature increases from 240 K to 270 K, the competition between magnetocrystalline anisotropy and FM becomes weaker due to more intense thermal disturbance, which results in the value of ρ_{xy}^T gradually decreases from 0.36 μΩ·cm to 0.04 μΩ·cm.

In summary, we reported the magnetization, magnetic domain and transport properties of the polycrystalline $Mn_{2.1}Fe_{0.9}Sn$ compound with hexagonal structure. The result of in-situ Lorentz transmission electron microscopy cooling experiment at zero field confirms the coexistence of spontaneous type-II magnetic bubbles owing a pair of Bloch lines and biskyrmion consisting of two skyrmions of opposite spin helicities in the sample. Topological Hall effect has been found in the range of measured temperature from 50 K to 270 K, and the maximum value of ρ_{xy}^T is about 9 μΩ·cm at 50 K. The reason of that is the formation of noncoplanar spin textures at low temperature due to the competition among magnetocrystalline anisotropy, antiferromagnetic coupling and ferromagnetic interaction.

Declaration of Competing Interest

The authors declare that they have no known competing financial interests or personal relationships that could have appeared to influence the work reported in this paper.

Acknowledgment

This work was supported by the National Key Research and Development Program of China (Grant No. 2016YFB0700903, 2017YFA0206300, 2016YFA0300701), the National Natural Science Foundation of China (Grant No. 51590881, 11520101002) and the Key Program of the Chinese Academy of Sciences of China(Grant No. QYZDY-SSW-SLH020, 112111KYSB20180013).

References

[1] S. Mühlbauer, B. Binz, F. Jonietz, C. Pfleiderer, A. Rosch, A. Neubauer, R. Georgii, P. Böni, Science 323 (2009) 915–919.
[2] X.Z. Yu, Y. Onose, N. Kanazawa, J.H. Park, J.H. Han, Y. Matsui, N. Nagaosa, Y. Tokura, Nature 465 (2010) 901–904.
[3] X.Z. Yu, N. Kanazawa, Y. Onose, K. Kimoto, W.Z. Zhang, S. Ishiwata, Y. Matsui, Y. Tokura, Nat. Mater. 10 (2011) 106–109.
[4] X.Z. Yu, M. Mostovoy, Y. Tokunaga, W.Z. Zhang, K. Kimoto, Y. Matsui, Y. Kaneko, N. Nagaosa, Y. Tokura, Proc. Natl. Acad. Sci. USA 109 (2012) 8856.
[5] X.Z. Yu, Y. Tokunaga, Y. Kaneko, W.Z. Zhang, K. Kimoto, Y. Matsui, Y. Taguchi, Y. Tokura, Nat. Commun. 5 (2014) 3198.
[6] W.H. Wang, Y. Zhang, G.Z. Xu, L.C. Peng, B. Ding, Y. Wang, Z.P. Hou, X.M. Zhang, X.Y. Li, E.K. Liu, S.G. Wang, J.W. Cai, F.W. Wang, J.Q. Li, F.X. Hu, G.H. Wu, B.G. Shen, X.X. Zhang, Adv. Mater. 28 (2016) 6887–6893.
[7] Z.P. Hou, W.J. Ren, B. Ding, G.Z. Xu, Y. Wang, B. Yang, Q. Zhang, Y. Zhang, E.K. Liu, F. Xu, W.H. Wang, G.H. Wu, X.X. Zhang, B.G. Shen, Z.D. Zhang, Adv. Mater. 29 (2017) 1701144.
[8] S.L. Zuo, M. Zhang, R. Li, Y. Zhang, L.C. Peng, J.F. Xiong, D. Liu, T.Y. Zhao, F.X. Hu, B.G. Shen, J.R. Sun, Acta Mater. 140 (2017) 465–471.
[9] S.L. Zuo, Y. Zhang, L.C. Peng, X. Zhao, R. Li, H. Li, J.F. Xiong, M. He, T.Y. Zhao, J.R. Sun, F.X. Hu, B.G. Shen, Nanoscale 10 (2018) 1039.
[10] S. Nakatsuji, N. Kiyohara, T. Higo, Nature 527 (2015) 212–215.
[11] T.F. Duan, W.J. Ren, W.L. Liu, S.J. Li, W. Liu, Z.D. Zhang, Appl. Phys. Lett. 107 (2015) 082403.
[12] K. Kuroda, T. Tomita, M.-T. Suzuki, C. Bareille, A.A. Nugroho, P. Goswami, M. Ochi, M. Ikhlas, M. Nakayama, S. Akebi, R. Noguchi, R. Ishii, N. Inami, K. Ono, H. Kumigashira, A. Varykhalov, T. Muro, T. Koretsune, R. Arita, S. Shin, T. Kondo, S. Nakatsuji, Nat. Mater. 16 (2017) 1090–1095.
[13] H. Yang, Y. Sun, Y. Zhang, W.J. Shi, S.S.P. Parkin, B.H. Yan, New J. Phys. 19 (2017) 015008.
[14] M. Ikhlas, T. Tomita, T. Koretsune, M.-T. Suzuki, D. Nishio-Hamane, R. Arita, Y. Otani, S. Nakatsuji, Nat. Phys. 13 (2017) 1085–1090.
[15] X.K. Li, L.C. Xu, L.C. Ding, J.H. Wang, M.S. Shen, X.F. Lu, Z.W. Zhu, K. Behnia, Phys. Rev. Lett. 119 (2017) 056601.
[16] T. Higo, H.Y. Man, D.B. Gopman, L. Wu, T. Koretsune, O.M.J. Erve, Y.P. Kabanov, D. Rees, Y.F. Li, M.-T. Suzuki, S. Patankar, M. Ikhlas, C.L. Chien, R. Arita, R.D. Shull, J. Orenstein, S. Nakatsuji, Nat. Photonics 12 (2018) 73–78.
[17] X.F. Zhou, B.J. Song, X.Z. Chen, Y.F. You, S.Y. Ruan, H. Bai, W.J. Zhang, G.H. Ma, J.Q. Yao, F. Pan, Z.M. Jin, C. Song, Appl. Phys. Lett. 115 (2019) 182402.
[18] B.C. Sales, B. Saparov, M.A. McGuire, D.J. Singh, D.S. Parker, Sci. Rep. 4 (2014) 7024.
[19] O.Y. Vekilova, B. Fayyazi, K.P. Skokov, O. Gutfleisch, C. Echevarria-Bonet, J.M. Barandiarán, A. Kovacs, J. Fischbacher, T. Schrefl, O. Eriksson, H.C. Herper, Phys. Rev. B 99 (2019) 024421.
[20] T. Hori, H. Niida, Y. Yamaguchi, H. Kato, Y. Nakagawa, J. Magn. Magn. Mater. 90 & 91 (1990) 159–160.
[21] M.R. Felez, A.A. Coelho, S. Gama, J. Magn. Magn. Mater. 444 (2017) 280–283.
[22] L.C. Peng, Y. Zhang, D.S. Hong, B. Zhang, J.Q. Li, J.W. Cai, S.G. Wang, J.R. Sun, B.G. Shen, Appl. Phys. Lett. 113 (2018) 142408.
[23] T. Saito, S. Kamishima, IEEE T. Magn. 55 (2019) 2900104.
[24] N. Kumar, Y. Soh, Y.H. Wang, Y. Xiong, Phys. Rev. B 100 (2019) 214420.
[25] Z.H. Liu, A. Burigu, Y.J. Zhang, H.M. Jafri, X.Q. Ma, E.K. Liu, W.H. Wang, G.H. Wu, Scr. Mater. 143 (2018) 122–125.
[26] Y.Q. Li, B. Ding, X.T. Wang, H.W. Zhang, W.H. Wang, Z.Y. Liu, Appl. Phys. Lett. 113 (2018) 062406.
[27] Y. Huh, P. Kharel, A. Nelson, V.R. Shah, J. Pereiro, P. Manchanda, A. Kashyap, R. Skomski, D.J. Sellmyer, J. Phys.: Condens. Matter. 27 (2015) 076002.
[28] K.-I. Kobayashi, T. Kimura, H. Sawada, K. Terakura, Y. Tokura, Nature 395 (1998) 677–680.

[29] X. Wang, M. Liu, X.D. Shen, Z.H. Liu, Z.W. Hu, K. Chen, P. Ohresser, L. Nataf, F. Baudelet, H.-J. Lin, C.-T. Chen, Y.-L. Soo, Y.F. Yang, C.Q. Jin, Y.W. Long, Inorg. Chem. 58 (2019) 320–326.
[30] J.H. Mooij, Phys. Stat. Sol. 17 (1973) 521.
[31] Z.H. Liu, Y.J. Zhang, H.G. Zhang, X.J. Zhang, X.Q. Ma, Appl. Phys. Lett. 109 (2016) 032408.
[32] P.K. Rout, P.V.P. Madduri, S.K. Manna, A.K. Nayak, Phys. Rev. B 99 (2019) 094430.
[33] W.L. Zuo, S.L. Zuo, R. Li, T.Y. Zhao, F.X. Hu, J.R. Sun, X.F. Zhang, J.P. Liu, B.G. Shen, J. Alloys Compd. 695 (2017) 1786–1792.
[34] H.R. Zhang, Y. Yun, X.J. Zhang, H. Zhang, Y. Ma, X. Yan, F. Wang, G. Li, R. Li, T. Khan, Y.S. Chen, W. Liu, F.X. Hu, B.G. Liu, B.G. Shen, W. Han, Jirong Sun, Phys. Rev. Lett. 121 (2018) 116803.
[35] H. Li, B. Ding, J. Chen, Z.F. Li, Z.P. Hou, E.K. Liu, H.W. Zhang, X.K. Xi, G.H. Wu, W.H. Wang, Appl. Phys. Lett. 114 (2019) 192408.